REPORT

2D MAGNETISM

Direct observation of van der Waals stacking–dependent interlayer magnetism

Weijong Chen[1], Zeyuan Sun[1], Zhongjie Wang[1], Lehua Gu[1], Xiaodong Xu[2], Shiwei Wu[1,3]*, Chunlei Gao[1,3]*

Controlling the crystal structure is a powerful approach for manipulating the fundamental properties of solids. In van der Waals materials, this control can be achieved by modifying the stacking order through rotation and translation between the layers. Here, we observed stacking-dependent interlayer magnetism in the two-dimensional (2D) magnetic semiconductor chromium tribromide ($CrBr_3$), which was enabled by the successful growth of its monolayer and bilayer through molecular beam epitaxy. Using in situ spin-polarized scanning tunneling microscopy and spectroscopy, we directly correlate the atomic lattice structure with the observed magnetic order. Although the individual monolayer $CrBr_3$ is ferromagnetic, the interlayer coupling in bilayer depends on the stacking order and can be either ferromagnetic or antiferromagnetic. Our observations pave the way for manipulating 2D magnetism with layer twist angle control.

The type of van der Waals (vdW) stacking has been extensively recognized as a critical component in determining the properties of layered vdW materials. In particular, weak interlayer vdW interactions allow for the control over the rotational and translational degrees of freedom between layers, creating a host of new materials with distinct stacking symmetries and functionalities (*1*–*3*). Whereas most previous work has focused on the electronic and optical properties associated with the vdW stacking (*4*–*7*), the recent discovery of magnetism in two-dimensional (2D) materials, achieved through both mechanical exfoliation (*8*–*13*) and molecular beam epitaxy (MBE) (*14*, *15*), provides an exciting opportunity to explore the effects of stacking order on a material's magnetic properties.

Among the 2D magnetic materials discovered so far, the family of chromium trihalides, CrX_3 (where X = Cl, Br, or I), has garnered special interest (*8*, *16*). For instance, ferromagnetism perpendicular to the 2D plane persists in monolayer CrI_3, whereas its bilayer exhibits interlayer antiferromagnetism. These magnetic structures lead to a number of emerging phenomena, such as giant tunneling magnetoresistance in spin-filter magnetic tunnel junctions (*17*–*19*), the electrical control of 2D magnetism (*20*–*22*), and giant nonreciprocal optical second-harmonic generation (*23*). In contrast to CrI_3, recent tunneling measurements suggest that the interlayer coupling in atomically thin $CrBr_3$ is ferromagnetic (*24*). This was confirmed through polar reflectance magnetic circular dichroism (RMCD) measurements of mechanically exfoliated bilayers of $CrBr_3$, which reveal magnetic hysteresis behavior centered around zero applied magnetic field, distinct from the three-step staircase pattern observed in bilayer CrI_3 (fig. S1). Given that CrI_3 and $CrBr_3$ are isostructural (*25*), such a substantial difference in the magnetic properties between their bilayers prompts a thorough investigation of the mechanisms governing the interlayer magnetic coupling (*26*).

Here, we used in situ spin-polarized scanning tunneling microscopy and spectroscopy (*27*, *28*) to establish a direct correlation between the interlayer magnetic coupling and the stacking structures in bilayer $CrBr_3$. The $CrBr_3$ films were grown on freshly cleaved, highly oriented pyrolytic graphite (HOPG) substrates by MBE. During the growth, the sample surface was monitored in situ by reflection high-energy electron diffraction (RHEED). Figure 1, A and B, respectively, show the RHEED patterns before and after growing $CrBr_3$ with the diffraction orders indicated. The stripe-like RHEED pattern from the $CrBr_3$ indicates the formation of a 2D crystalline thin film, confirmed by scanning tunneling microscopy (STM) to be a monolayer $CrBr_3$ (Fig. 1C). Further deposition of $CrBr_3$ led to the appearance of bilayer $CrBr_3$ islands (Fig. 1D) [for details about the MBE growth, see (*29*)].

Figure 1E shows the atomically resolved STM image of the monolayer $CrBr_3$, revealing periodically spaced triangular cluster protrusions. To understand this image, we consider the monolayer crystal structure of $CrBr_3$. As shown in Fig. 1F, Cr atoms are arranged in a honeycomb lattice structure, and each atom is surrounded by an octahedron of six Br atoms (*16*). Within a single honeycomb formed by six Cr atoms, there are three Br atoms at the top and bottom surfaces, marked by solid and dotted green triangles with opposite orientations, respectively. Thus, the monolayer $CrBr_3$ has three-fold rotational symmetry, with the rotational axis across either the Cr atoms or the center of the honeycomb. By overlaying the atomic structure on top of the STM image in Fig. 1E, we determined that the observed triangular cluster is formed by the three top Br atoms (solid green triangle in Fig. 1E). The measured in-plane lattice constant is 6.3 Å, consistent with the bulk lattice constant (6.26 Å) (*25*). The monolayer thickness is determined to be 6.5 Å by atomic force microscopy (AFM), as shown in Fig. 1G. Structural domains and their boundaries are also clearly seen in the image. Both the large-scale topography and the atomically resolved STM images demonstrate the high-quality growth of the monolayer $CrBr_3$ films.

To measure the magnetic properties, we performed in situ spin-polarized STM measurements with an applied out-of-plane magnetic field at 5 K [for spin-polarized STM measurements, see (*29*)]. We used antiferromagnetic Cr-coated tungsten tips in which magnetization at the tip apex remained stable while the external magnetic field was swept (*30*). Figure 2A shows the tunneling spectra (dI/dV) from a monolayer $CrBr_3$ with oppositely applied fields (B = ±0.3 T), measured on the center of a Br triangular cluster. Although both dI/dV curves show semiconducting behavior near zero bias voltage, they clearly differ at some bias voltage V_b, which results from the magnetization flip of the monolayer $CrBr_3$ under the reversal of the external magnetic field. To further confirm the existence of ferromagnetism, we measured a series of dI/dV spectra while sweeping the magnetic field back and forth. Figure 2B plots the hysteresis loop at V_b = 1.4 V. Additional data at different bias voltages are shown in fig. S2. A rectangular hysteresis loop was observed with a coercive field of ~30 mT, with the two dI/dV plateaus corresponding to different magnetization states (spin up or spin down). This observation suggests that epitaxial $CrBr_3$ monolayers grown on HOPG are semiconducting ferromagnets with a well-defined, out-of-plane easy axis. The dI/dV plateaus have sensitive dependence on bias voltages, atomic sites, and Cr tips (see figs. S2 and S3) because the dI/dV signal is determined by the spin- and energy-dependent local density of states of the tip and the sample (*29*).

[1]State Key Laboratory of Surface Physics, Key Laboratory of Micro and Nano Photonic Structures (MOE), Department of Physics, and Institute for Nanoelectronic Devices and Quantum Computing, Fudan University, Shanghai 200433, China. [2]Department of Physics and Department of Materials Science and Engineering, University of Washington, Seattle, WA 98195, USA. [3]Collaborative Innovation Center of Advanced Microstructures, Nanjing 210093, China.
*Corresponding author. Email: clgao@fudan.edu.cn (C.G.); swwu@fudan.edu.cn (S.W.)

Downloaded from http://science.sciencemag.org/ on November 21, 2019

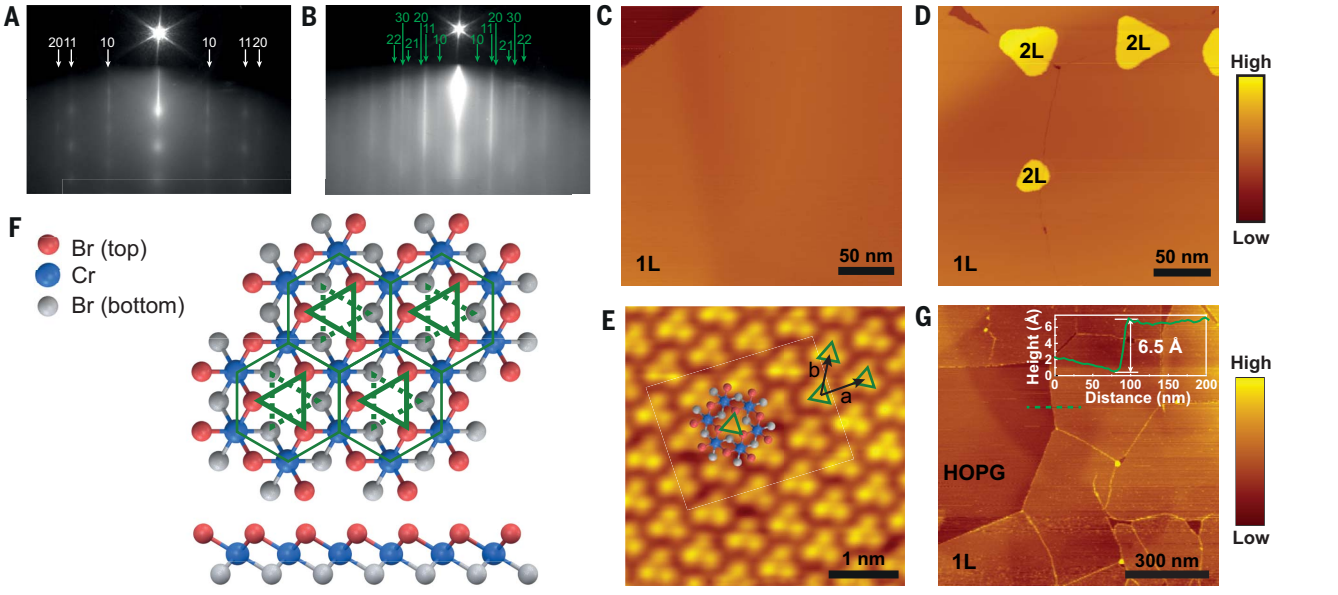

Fig. 1. MBE Growth of $CrBr_3$ monolayer and bilayer on HOPG. (**A** and **B**) RHEED patterns with indicated diffraction orders of (A) the bare HOPG substrate and (B) the MBE-grown $CrBr_3$ film. (**C** and **D**) STM images of (C) the $CrBr_3$ monolayer with (D) bilayer islands. The scan parameters were as follows: V_b = 1.1 V, I = 100 pA, T = 5 K for (C) and V_b = 1.5 V, I = 100 pA, T = 5 K for (D). (**E**) Atomically resolved image of a monolayer $CrBr_3$ with an overlaid atomic structure. The scan parameters were as follows: V_b = 1.5 V, I = 500 pA, T = 5 K. The lattice constants were determined to be 6.3 Å for the primitive vectors **a** and **b**, consistent with the bulk values. (**F**) Illustrations of the top and side views of the monolayer $CrBr_3$ atomic structure. The Cr atoms form a honeycomb lattice sandwiched by Br atoms. Within the Cr honeycomb lattice, the top and bottom surfaces of Br atoms form single triangles but with opposite orientation, indicated by solid and dotted green lines, respectively. (**G**) AFM image of monolayer $CrBr_3$ with partial coverage. A line-cut profile across the monolayer and bare substrate is shown with a monolayer height of ~6.5 Å.

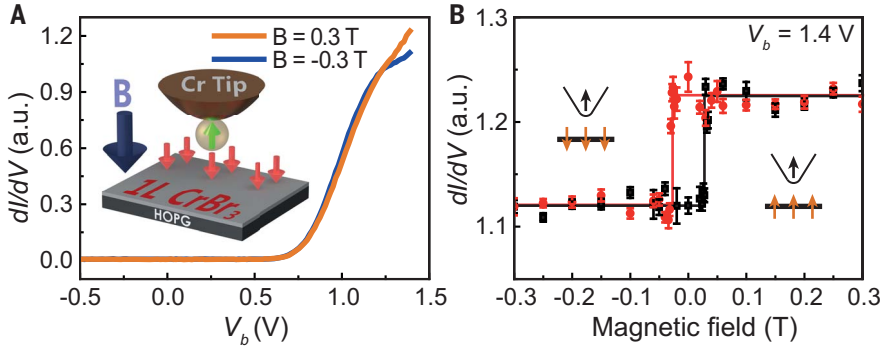

Fig. 2. Spin-polarized tunneling of monolayer $CrBr_3$. (**A**) Spin-polarized tunneling spectra under positive and negative out-of-plane magnetic fields (±0.3 T). The inset illustrates the experimental geometry. The magnetization at the tip apex is assumed to be spin up, and the same assumption applies to the following figures [see discussion in (*29*)]. (**B**) *dI/dV* signal as a function of the magnetic field. V_b was fixed at 1.4 V. The out-of-plane magnetic field was swept upward (black data) and downward (red data). The ferromagnetic hysteresis loop is outlined as rectangular solid lines. Insets sketch the two configurations of the magnetization alignment between the Cr tip and the monolayer $CrBr_3$ film. The in-plane component of magnetization at the Cr tip apex, if any, does not contribute to the magnetic contrast in *dI/dV*.

With the atomic structure of monolayer $CrBr_3$ determined and its ferromagnetism confirmed, we now focus on bilayer $CrBr_3$. In general, there are two types of stacking structures with the unit cell size the same as that of the monolayer: the R-type, with both layers aligned to the same orientation, and the H-type, with a 180° rotation between the layers. For R-type stacking, two polytypes for $CrBr_3$ bulk crystals were reported: rhombohedral at low temperature and monoclinic at high temperature (>420 K) (*16*). These two structures mainly differ in the relative translation between the two monolayers. However, common to vdW materials (*4*, *5*, *31*), the energy differences between different stacking structures can be relatively small, even if the stacking structure is absent in bulk crystal. Therefore, the possible stacking structures in the bilayer case could be far more complex than the two reported in the literature. By only considering the high-symmetry configurations (i.e., hollow, bridge, and top sites) between the halogen atoms at the interface of adjacent layers, there are already six and five polytypes for R-type stacking (table S1) and H-type stacking (table S2), respectively.

We found that the H- and R-type stacking structures can both form in the MBE-grown bilayers and they give rise to distinct interlayer magnetic coupling. The results corresponding to the H-type stacking structure are given in Fig. 3. Figure 3A shows the STM image across the step edge between a bilayer $CrBr_3$ island and a monolayer $CrBr_3$ film that is an extension of the bilayer's bottom layer. Their atomically resolved STM images are shown in Fig. 3, B and C, which show individual triangular clusters formed by the top three Br atoms in the unit cell of $CrBr_3$, similar to those in Fig.

Downloaded from http://science.sciencemag.org/ on November 21, 2019

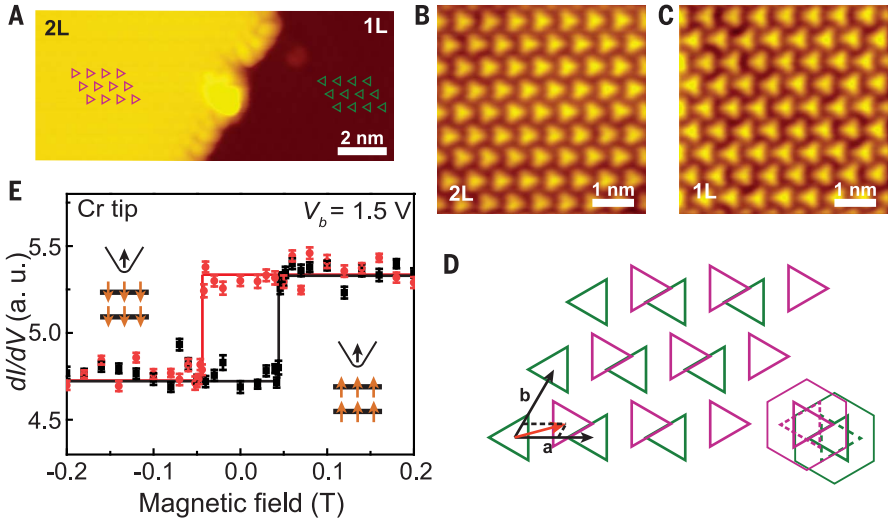

Fig. 3. Interlayer ferromagnetic coupling in an H-type stacked bilayer $CrBr_3$. (**A**) STM image of a $CrBr_3$ film with both a monolayer (1L) region and a bilayer (2L) island. (**B** and **C**) Magnified, atomically resolved images of (B) the bilayer region and (C) its extended bottom monolayer at V_b = 1.9 V, indicating that the top and bottom layers in the bilayer are anti-aligned, or rotated by 180° (H-type stacking). (**D**) Atomic structure of the bilayer $CrBr_3$, as determined from atomically resolved STM images (for further details, see fig. S4). The unit cells of the top and bottom layers are represented by the magenta and green solid triangles, respectively, corresponding to the top surface of Br atoms in each monolayer sheet. These magenta and green solid triangles are also overlaid on the monolayer and bilayer in (A). The unit cell of the top layer (magenta) is a translation by 0.55**a** + 0.20**b** of the bottom layer (green). For comparison with the structures in table S2, the stacking structure is also shown with the bottom surface of Br atoms of each monolayer sheet as dotted triangles and the Cr atoms as solid hexagons. (**E**) Spin-polarized tunneling on the bilayer $CrBr_3$ as a function of magnetic field with a Cr tip at V_b = 1.5 V. The out-of-plane magnetic field was swept upward (black data) and downward (red data). Like that of the monolayer $CrBr_3$, a rectangular ferromagnetic hysteresis loop was observed with a coercive field of ~45 mT. Insets depict two configurations of the magnetization alignment between the tip and the sample.

1E. The orientation of the triangular clusters from the monolayer region, which has the same crystal structure as the bottom layer of the bilayer, is exactly opposite to the top layer in the bilayer, suggesting H-type stacking.

To determine the translational degree of freedom between the two layers, we overlaid the two $CrBr_3$ lattices, represented by the magenta and green triangles, on the top and bottom layers of the bilayer island shown in Fig. 3A (for further details, see fig. S4). We found that the top layer is translated to 0.55**a** + 0.20**b** with respect to the bottom layer (Fig. 3D). Given that the experimental uncertainty of translation is ~±7% of the lattice constants **a** and **b**, the closest stacking structure is "bridge I" of H-type stacking listed in table S2. We also observed the equivalent bridge I structure, in which the top layer is translated to 0.76**a** + 0.38**b** of the bottom layer (fig. S5). In terms of both rotational and translational degrees of freedom, this observed stacking structure is distinct from the reported structure models for CrX_3 in the literature (*16*, *25*). Further spin-polarized STM measurement on this H-type stacked bilayer $CrBr_3$ showed a rectangular magnetic hysteresis loop with a coercive magnetic field of ~45 mT (Fig. 3E for V_b = 1.5 V and fig. S6 for other bias voltages), similar to the hysteresis observed in $CrBr_3$ monolayers (Fig. 2B). Thus, in H-type stacked bilayer $CrBr_3$, the interlayer coupling is ferromagnetic.

The second kind of stacking structure is depicted in Fig. 4, where the triangular clusters from the adjacent monolayer and bilayer regions are oriented in the same direction (Fig. 4, A to C), suggesting R-type stacking. The translational degree of freedom between the two layers is determined in the same way as in Fig. 3. In R-type stacking, the top layer is translated to 0.48**a** + 0.48**b** with respect to the bottom layer (Fig. 4D; for further analysis details, see fig. S7). In one R-type–stacking sample, we also observed that the top layer was translated to 0.21**a** + 0.78**b** of the bottom layer (fig. S8). Examining their stacking structures, we found that they are close to the structures named "special" and "bridge I" listed in table S1. As illustrated in fig. S9, both structures share the same lattice symmetry (C_{2h}) as the monoclinic structure (*16*), but with a translation along the mirror plane.

For the R-type stacked bilayer, we observed four plateaus in the hysteresis loop when a Cr tip was used (Fig. 4E and fig. S10), distinct from the two plateaus observed on the $CrBr_3$ monolayer and the H-type stacked bilayer. This four-plateau behavior suggests that the R-type stacked bilayer is antiferromagnetically coupled in its ground states, giving rise to two additional magnetization configurations. Above +0.5 T or below −0.5 T, the magnetization direction of the bilayer $CrBr_3$ is aligned to the same direction by the external magnetic field. As in the ferromagnetic $CrBr_3$ monolayer and bilayer, the parallel or antiparallel alignment between the tip and the sample yields two different dI/dV plateaus. Within ±0.5 T, the individual ferromagnetic layers are antiferromagnetic coupled, which creates an additional magnetic tunnel junction across the vdW gap. Depending on how the spin direction of the top layer aligns with the Cr tip, two new magnetization configurations are formed (inset of Fig. 4E).

The interlayer antiferromagnetism in R-type stacked bilayer $CrBr_3$ is further corroborated with a nonmagnetic W tip under external magnetic field. Figure 4F shows such a measurement on another R-type stacked bilayer at V_b = 1.5 V (see fig. S11 for data with different bias voltages). Starting with zero applied magnetic field, sweeping the external magnetic field in either direction results in a plateau in the dI/dV curve. Beyond magnetic fields of ±0.5 T, the dI/dV abruptly changes (Fig. 4F). Although the relative magnitude of dI/dV plateaus depends on bias voltage, the two-plateau behavior demonstrates the magnetic field–driven transition from antiferromagnetic to ferromagnetic interlayer coupling. Such tunneling magnetoresistance behavior was recently discovered in spin-filter magnetic tunnel junctions using mechanically exfoliated bilayer CrI_3 (*17*–*19*). By contrast, when a nonmagnetic W tip was used for H-type stacked bilayers that were ferromagnetically coupled, no magnetic field–dependent dI/dV features at any bias voltage could be observed (fig. S12). In addition to the dI/dV magnetic contrast, the antiferromagnetic ground state in this R-type stacked bilayer could be captured in the contrast of STM height driven under external magnetic field, as shown in fig. S13.

The distinct interlayer magnetism, from antiferromagnetic coupling in R-type stacking to ferromagnetic coupling in H-type stacking, in our MBE-grown bilayer $CrBr_3$ clearly demonstrates the substantial tunability of 2D magnetism through the stacking order. The interlayer coupling in bilayer $CrBr_3$ is mediated through a superexchange interaction, which is controlled by the directional hybridization

Downloaded from http://science.sciencemag.org/ on November 21, 2019

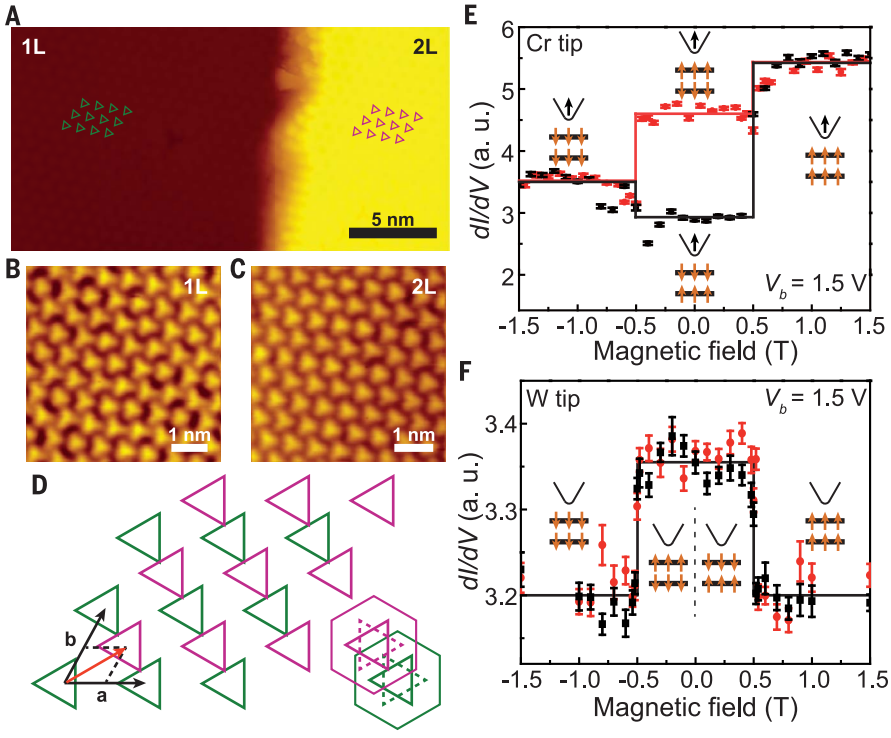

Fig. 4. Interlayer antiferromagnetic coupling in an R-type stacked bilayer $CrBr_3$. (**A**) STM image of a $CrBr_3$ film with both a monolayer (1L) region and a bilayer (2L) island. (**B** and **C**) Atomically resolved images of (B) the monolayer and (C) the bilayer. V_b = 1.9 V. The stacking configuration in the bilayer is identified as R-type, i.e., the top and bottom layers are in the same orientation. (**D**) Atomic structure of the bilayer $CrBr_3$, as determined from atomically resolved STM images (see fig. S7 for further details). The representation style follows that in Fig. 3. The unit cell of the top layer (magenta) is translated by 0.48**a** + 0.48**b** from the bottom layer (green). (**E**) Spin-polarized tunneling on an R-type stacked bilayer $CrBr_3$ with a Cr tip at V_b = 1.5 V. The insets show four magnetization configurations, including the Cr tip and bilayer $CrBr_3$, corresponding to different magnetic field–dependent *dI*/*dV* plateaus. The out-of-plane magnetic field was swept upward (black data) and downward (red data). (**F**) Spin-dependent tunneling on the bilayer $CrBr_3$ in (C) with a nonmagnetic W tip at V_b = 1.5 V. Abrupt decrease of the *dI*/*dV* signal was observed at magnetic fields of ~±0.5 T, suggesting an interlayer antiferromagnetic coupling within ±0.5 T.

between the Br p-orbitals and Cr d-orbitals (*32*, *33*). Because the bond angles and the bond distances of the Cr–Br–Br–Cr exchange path are strongly dependent on the stacking order, the interlayer magnetism is expected to also depend on the specific stacking structure, including the interlayer distance and atomic site positions. In fact, recent theoretical studies have investigated the interlayer magnetism of the rhombohedral and monoclinic structures in bilayer CrI_3 (*34*–*37*).

Although the exact growth mechanism remains to be investigated, our observations illustrate the polytypism in vdW materials and its importance to 2D magnetism. Our work also calls for a close examination for the stacking structures in mechanically exfoliated CrX_3 samples, as the exfoliated bilayer CrI_3 and $CrBr_3$ exhibit distinct interlayer magnetic coupling. We envision that this working principle could be used to manipulate 2D magnetism, for example, by engineering spatially dependent spin textures uniquely enabled by twisted bilayers and heterostructures (*38*).

REFERENCES AND NOTES

1. A. K. Geim, I. V. Grigorieva, *Nature* **499**, 419–425 (2013).
2. K. S. Novoselov, A. Mishchenko, A. Carvalho, A. H. Castro Neto, *Science* **353**, aac9439 (2016).
3. R. Ribeiro-Palau *et al.*, *Science* **361**, 690–693 (2018).
4. W. Bao *et al.*, *Nat. Phys.* **7**, 948–952 (2011).
5. C. H. Lui, Z. Li, K. F. Mak, E. Cappelluti, T. F. Heinz, *Nat. Phys.* **7**, 944–947 (2011).
6. Y. Shan *et al.*, *Sci. Adv.* **4**, eaat0074 (2018).
7. T. Jiang *et al.*, *Nat. Nanotechnol.* **9**, 825–829 (2014).
8. B. Huang *et al.*, *Nature* **546**, 270–273 (2017).
9. C. Gong *et al.*, *Nature* **546**, 265–269 (2017).
10. Z. Fei *et al.*, *Nat. Mater.* **17**, 778–782 (2018).
11. Y. Deng *et al.*, *Nature* **563**, 94–99 (2018).
12. J. U. Lee *et al.*, *Nano Lett.* **16**, 7433–7438 (2016).
13. X. Wang *et al.*, *2D Mater.* **3**, 031009 (2016).
14. D. J. O'Hara *et al.*, *Nano Lett.* **18**, 3125–3131 (2018).
15. M. Bonilla *et al.*, *Nat. Nanotechnol.* **13**, 289–293 (2018).
16. M. A. McGuire, H. Dixit, V. R. Cooper, B. C. Sales, *Chem. Mater.* **27**, 612–620 (2015).
17. T. Song *et al.*, *Science* **360**, 1214–1218 (2018).
18. D. R. Klein *et al.*, *Science* **360**, 1218–1222 (2018).
19. Z. Wang *et al.*, *Nat. Commun.* **9**, 2516 (2018).
20. S. Jiang, J. Shan, K. F. Mak, *Nat. Mater.* **17**, 406–410 (2018).
21. B. Huang *et al.*, *Nat. Nanotechnol.* **13**, 544–548 (2018).
22. S. Jiang, L. Li, Z. Wang, K. F. Mak, J. Shan, *Nat. Nanotechnol.* **13**, 549–553 (2018).
23. Z. Sun *et al.*, *Nature* **572**, 497–501 (2019).
24. D. Ghazaryan *et al.*, *Nature Electronics* **1**, 344–349 (2018).
25. M. McGuire, *Crystals (Basel)* **7**, 121 (2017).
26. L. Thiel *et al.*, *Science* **364**, 973–976 (2019).
27. R. Wiesendanger, *Rev. Mod. Phys.* **81**, 1495–1550 (2009).
28. M. Bode, *Rep. Prog. Phys.* **66**, 523–582 (2003).
29. See supplementary materials for additional information.
30. R. Wiesendanger *et al.*, *J. Magn. Magn. Mater.* **272**, 2115–2120 (2004).
31. M. Chhowalla *et al.*, *Nat. Chem.* **5**, 263–275 (2013).
32. J. L. Lado, J. Fernández-Rossier, *2D Mater.* **4**, 035002 (2017).
33. W. B. Zhang, Q. Qu, P. Zhua, C. H. Lam, *J. Mater. Chem. C Mater. Opt. Electron. Devices* **3**, 12457–12468 (2015).
34. P. Jiang *et al.*, *Phys. Rev. B* **99**, 144401 (2019).
35. D. Soriano, C. Cardoso, J. Fernández-Rossier, *Solid State Commun.* **299**, 113662 (2019).
36. N. Sivadas, S. Okamoto, X. Xu, C. J. Fennie, D. Xiao, *Nano Lett.* **18**, 7658–7664 (2018).
37. S. W. Jang, M. Y. Jeong, H. Yoon, S. Ryee, M. J. Han, *Phys. Rev. Mater.* **3**, 031001(R) (2019).
38. Q. Tong, F. Liu, J. Xiao, W. Yao, *Nano Lett.* **18**, 7194–7199 (2018).
39. W. Chen *et al.*, Replication data for: Direct observation of van der Waals stacking-dependent interlayer magnetism, version 1.0, Zenodo (2019).

ACKNOWLEDGMENTS

We thank D. Xiao and T. Cao for insightful discussion, B. Huang for proofreading the paper, and D. Feng for lending the AFM. **Funding:** The work at Fudan was supported by the National Key Research and Development Program of China (grant nos. 2016YFA0300904 and 2016YFA0301002), the National Basic Research Program of China (grant no. 2014CB921601), and the National Natural Science Foundation of China (grant nos. 11427902 and 11674063). X.X. is supported by the Department of Energy, Basic Energy Sciences, Materials Sciences and Engineering Division (DE-SC0018171). **Author contributions:** C.G. and S.W. conceived and supervised the project. W.C. grew the sample and conducted the STM experiment with the assistance from Z.W. Z.S. conducted the RMCD measurement. L.G. and W.C. conducted the AFM measurement. W.C., Z.S., X.X., S.W., and C.G. analyzed the data and wrote the paper. **Competing interests:** The authors declare no competing interests. **Data and materials availability:** All data discussed in this paper are available at Zenodo (*39*).

SUPPLEMENTARY MATERIALS

science.sciencemag.org/content/366/6468/983/suppl/DC1
Materials and Methods
Figs. S1 to S17
Tables S1 and S2
References (*40*–*42*)

23 August 2018; resubmitted 20 February 2019
Accepted 25 October 2019
10.1126/science.aav1937

Downloaded from http://science.sciencemag.org/ on November 21, 2019

Science

Direct observation of van der Waals stacking–dependent interlayer magnetism

Weijong Chen, Zeyuan Sun, Zhongjie Wang, Lehua Gu, Xiaodong Xu, Shiwei Wu and Chunlei Gao

Science **366** (6468), 983-987.
DOI: 10.1126/science.aav1937

Stacking control

Recent searches for two-dimensional magnets have turned up a number of related van der Waals materials, such as chromium triiodide (CrI_3) and chromium tribromide ($CrBr_3$). Although their properties are expected to be similar, in bilayer form, the former is antiferromagnetic, whereas the latter appears to be a ferromagnet. Chen *et al.* used spin-polarized scanning tunneling microscopy to determine that the nature of the magnetic state in bilayer $CrBr_3$ depends on the type of stacking of its monolayers. An antiferromagnetic state formed when the two monolayers were oriented in the same direction, whereas the opposite orientation led to ferromagnetism.

Science, this issue p. 983

ARTICLE TOOLS http://science.sciencemag.org/content/366/6468/983

SUPPLEMENTARY MATERIALS http://science.sciencemag.org/content/suppl/2019/11/20/366.6468.983.DC1

REFERENCES This article cites 42 articles, 6 of which you can access for free
http://science.sciencemag.org/content/366/6468/983#BIBL

PERMISSIONS http://www.sciencemag.org/help/reprints-and-permissions

Use of this article is subject to the Terms of Service

Science (print ISSN 0036-8075; online ISSN 1095-9203) is published by the American Association for the Advancement of Science, 1200 New York Avenue NW, Washington, DC 20005. The title *Science* is a registered trademark of AAAS.

Copyright © 2019 The Authors, some rights reserved; exclusive licensee American Association for the Advancement of Science. No claim to original U.S. Government Works

Downloaded from http://science.sciencemag.org/ on November 21, 2019